Editors' Suggestion

Cooling Mechanism Controls Motility-Induced Phase Separation in Inertial Active Liquids

Manuel Mayo,[1] Lorenzo Caprini,[2] María Isabel García de Soria,[1] Umberto Marini Bettolo Marconi,[3] Pablo Maynar,[1] Luca Pizzoli,[2] and Andrea Puglisi[4,2,5,*]

[1]*Física Teórica, Universidad de Sevilla, Apartado de Correos 1065, E-41080 Sevilla, Spain*
[2]*Sapienza University of Rome, Physics Department, Piazzale Aldo Moro 2, Rome, Italy*
[3]*School of Sciences and Technology, University of Camerino, Via Madonna delle Carceri, Camerino, Italy*
[4]*Istituto dei Sistemi Complessi - Consiglio Nazionale delle Ricerche, P.le A. Moro 2, Rome, Italy*
[5]*INFN, Sezione Roma2, Via della Ricerca Scientifica 1, I-00133, Rome, Italy*

(Received 24 November 2025; accepted 8 April 2026; published 8 May 2026)

Motility-induced phase separation (MIPS) is a central collective phenomenon in active matter, theoretically established in the overdamped regime. We discover that the dynamical origin of MIPS is fundamentally altered by inertia, which induces a cooling mechanism absent in overdamped active matter. This conclusion is supported by an active variant of the direct simulation Monte Carlo method and by a kinetic theory for inertial self-propelled hard spheres derived from the microscopic dynamics. In contrast to the overdamped case, both analyses demonstrate that inertial MIPS can occur even without impenetrability, as it originates from a density-dependent cooling mechanism due to the coupling of density, orientation, and temperature. This mechanism emerges from the competition between activity and a density-dependent collision rate arising from spatial correlations between colliding particles. These findings open a pathway to fundamentally connect inertial active matter with granular physics.

DOI: 10.1103/mbrl-v75b

Introduction—Active matter [1–3] encompasses a broad class of systems. At submicron scales, it includes intracellular proteins, filaments, and organelles [4]. On the micron scale, active systems range from sperm cells [5] and bacteria [6,7] to synthetic active colloids [8,9]. Active matter is also ubiquitous at macroscopic scales and can be encountered in everyday life, from animal groups [10] and pedestrian crowds [11] to granular robots [12,13] and drone swarms [14]. The defining feature of these systems is an internal mechanism of energy injection that drives them far from thermodynamic equilibrium [15], for example, by sustaining self-propelled motion.

Active materials can self-organize even under conditions where passive matter remains disordered. A striking example is motility-induced phase separation (MIPS) [16–18], a nonequilibrium coexistence between dense and dilute phases [19–23]. This phase separation can arise either from quorum sensing [16] or from the interplay between persistent self-propulsion and volume exclusion, specifically, particle impenetrability. In the latter case, active particles in the overdamped regime move at constant velocity and block each other upon collisions, generating a density-dependent active speed [24]. This slowdown promotes cluster nucleation even in the absence of attractive interactions [25–28]. MIPS has been extensively analyzed using nonequilibrium statistical mechanics, particularly in the overdamped regime, where kinetic energy rapidly relaxes to the bath temperature [24,29]. In this limit, MIPS can be described through an effective free-energy approach with a modified Maxwell construction [30] or via mechanical [31] and kinetic theories [32].

Understanding the role of inertia has become increasingly important, given the large variety of active systems observed at macroscopic scales [33], including polar granular particles powered by internal motors [34–37], grains driven by vibrating plates [38–43], granular spinners [44–47], whirling fruits [48], and flying beetles [49], typically operating in air where the Stokes time is on the order of seconds. In these systems, inertia cannot be neglected and influences both single-particle dynamics [50–54] and collective behavior [55–58]. In particular, inertia suppresses MIPS [59–61] and, through a bounce-back mechanism [62,63], generates a temperature difference between the dense cluster and the dilute phase [60]—a feature recently exploited to propose a nonequilibrium refrigerator [64]. Numerical studies also reveal oscillatory behaviors [65] and a nucleationlike MIPS [66] in contrast to the spinodal decomposition typical of overdamped active

*Contact author: andrea.puglisi@cnr.it

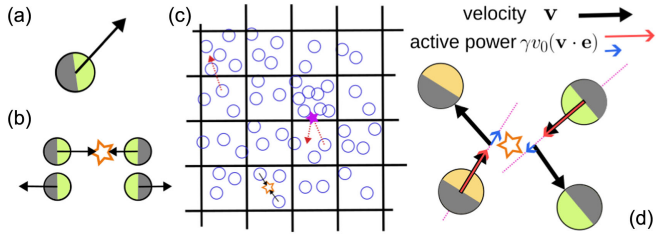

FIG. 1. Inertia-induced cooling in active systems. (a) Particles are endowed with both a velocity $\mathbf{v}$ (black arrow) and an active force $\gamma v_0 \mathbf{e}$ directed along the direction normal to the hemisphere, going from gray to color. (b) After a collision, velocities are instantaneously changed, while active forces remain unchanged. (c) In ADSMC, time and space are discretized. At each time step, the first phase is free motion (red arrow), and the second phase is interaction: pair collisions in the same cell (orange star) and (when implemented) "backscattering events" of single particles with overcrowded cells (purple star). (d) Collisional cooling effect. Cap colors identify the same particles before and after the collision. The modulus of the colored arrows represents the "active power" $\gamma v_0(\mathbf{v}\cdot\mathbf{e})$ (in $d=2$), which decreases after impact (from red to blue). Since $\gamma v_0(\mathbf{v}\cdot\mathbf{e})$ determines the value of the local temperature field, see Eq. (3), inertial active particles undergo an effective cooling mechanism during collisions.

systems [16]. These findings indicate that the mechanism underlying MIPS may differ fundamentally when inertia dominates as an effect of the temperature field. However, beyond a mechanical theory predicting the coexistence line [67], a comprehensive kinetic theory is still lacking, leaving open questions about the role of the temperature.

Here, we demonstrate that MIPS in inertial active systems originates from a cooling mechanism absent in the overdamped regime. The mechanism can be understood by considering a binary collision between two particles [Fig. 1(d)]. After the impact, the particle velocity is reflected, while the self-propulsion remains unchanged. The velocity then relaxes toward the self-propulsion over a finite inertial time, during which the particle speed is smaller than the free speed v_0. This reduces the kinetic energy [see Eq. (3)] and leads to a pressure inversion reminiscent of clustering in granular materials [68,69]. The cooling origin of inertial MIPS is confirmed by simulations performed with an active version of the direct Monte Carlo scheme (Bird algorithm) where impenetrability can be switched off. These findings are supported by a kinetic theory derived from the Boltzmann-Fokker-Planck equation for the microscopic dynamics, which predicts the onset of a linear instability driven by activity, inertia, and the Enskog correction to molecular chaos.

Model—We consider N active spheres of mass m and diameter σ, with positions $\mathbf{r}_i$ and velocities $\dot{\mathbf{r}}_i = \mathbf{v}_i$, evolving as

$$m\dot{\mathbf{v}}_i = \mathbf{f}_i^{\mathrm{int}} + \gamma v_0 \mathbf{e}_i - \gamma \mathbf{v}_i + \sqrt{2\gamma T_0}\boldsymbol{\eta}_i(t), \tag{1}$$

where $\gamma v_0 \mathbf{e}_i$ is the self-propulsion force and $\mathbf{f}_i^{\mathrm{int}}$ represents elastic hard-core interparticle collisions [Fig. 1(a)]; details of the implementation are given in the description of the numerical algorithm. The parameters γ and T_0 represent the drag coefficient and bath temperature, respectively, with Boltzmann's constant set to $k_B = 1$. Here, $\boldsymbol{\eta}_i(t)$ is a white noise vector with zero mean and unit variance. The self-propulsion vector $\mathbf{e}_i$ follows an active Ornstein-Uhlenbeck particle dynamics with autocorrelation time τ,

$$\tau\dot{\mathbf{e}}_i = -\mathbf{e}_i + \sqrt{2\tau}\boldsymbol{\xi}_i, \tag{2}$$

where $\boldsymbol{\xi}_i$ is a white noise vector with zero mean and unit variance, implying $\langle \mathbf{e}_i^2 \rangle = d$, where d is the space dimensionality. Two relevant dimensionless parameters are the Péclet number $\ell = \tau v_0/\sigma$ and the Stokes number $\mathrm{St} = m/(\gamma\tau)$ quantifying, respectively, the activity and the inertia of the system.

Particles move in a box of size L with periodic boundary conditions and interact through instantaneous collisions that change the velocities of particles i and j from $\mathbf{v}_i$, $\mathbf{v}_j$ to $\mathbf{v}_i'$, $\mathbf{v}_j'$, conserving kinetic energy and total momentum but leaving unchanged $\mathbf{e}_i$ and $\mathbf{e}_j$ [see Fig. 1(b) and End Matter (EM) for the exact collision rules]. Since collisions conserve kinetic energy, the evolution of $T = m\langle \mathbf{v}^2 \rangle/d$ in the homogeneous state (no macroscopic drifts and no spatial gradients) is dictated by the following equation obtained by averaging the Ito-transformation of Eq. (1):

$$\dot{T} = -(2\gamma/m)(T - T_0) + (2\gamma/d)v_0\langle \mathbf{v}\cdot\mathbf{e}\rangle. \tag{3}$$

The last term is the so-called *active power*, which quantifies the heating efficiency of self-propulsion: the randomizing effect of collisions reduces this term and produces an indirect local cooling of the system; see Fig. 1(d).

Active direct simulation Monte Carlo (ADSMC)—To explore the effects of the aforementioned cooling mechanism, the model is simulated through the ADSMC, i.e., a particle-based Monte Carlo method that accounts for self-propulsion [Fig. 1(c)]. Both time and space are discretized by choosing a time step dt and a cell size Δ smaller than the minimal time and length scales involved, yet large enough to allow statistical averaging; results are independent of dt and Δ within a reasonable range. At each time step, we evolve the free-streaming active trajectory [Eqs. (1) and (2) for $d=2$] and compute interactions by performing elastic collisions at random positions within each cell. The local collision frequency is estimated as proportional to $\chi(\phi)\sigma\phi\bar{v}$, where $\phi = n\pi\sigma^2/4$ is the local packing fraction (with n the local density) and $\bar{v}$ the typical velocity fluctuation inside the cell. The term $\chi(\phi)$ represents a correction accounting for positional correlations in non-dilute conditions. We consider two choices: (i) $\chi(\phi) = 1$, corresponding to pure molecular chaos, and (ii) $\chi(\phi)$ given by the Carnahan-Starling formula for the density

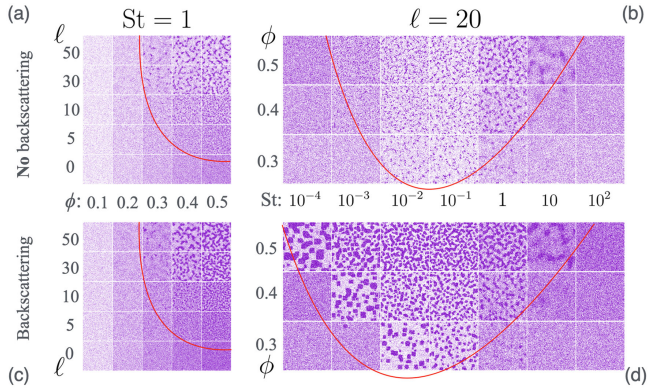

FIG. 2. Numerical results obtained using ADSMC with the Enskog collision rate. (a),(c) Snapshot phase diagrams in the plane of Péclet number ℓ and packing fraction ϕ at Stokes number $\mathrm{St} = 1$. (b),(d) Snapshot phase diagrams in the (ϕ, St) plane for $\ell = 20$. Panels (a) and (b) correspond to simulations without the backscattering effect (no impenetrability), while (c) and (d) include the backscattering effect (impenetrability). Red lines serve as guides to the eye. The remaining simulation parameter is $T_0 = 1$.

correlation at contact [70]. The latter choice is equivalent to an Enskog correction in kinetic theory, which does not explicitly account for impenetrability, as collisions occur at random positions within the cell. Additional simulations are performed using a backscattering mechanism [termed "BS," see Fig. 1(c)] to mimic impenetrability. (See the EM for details of the numerics).

Inertial MIPS—Simulations start with homogeneously distributed particle positions and Gaussian-distributed velocities. In some cases, the homogeneous distribution becomes unstable and develops spatial inhomogeneities with clusters, reminiscent of MIPS. This instability is never observed under pure molecular chaos [$\chi(\phi) = 1$] and occurs only when the Enskog correction is included. In this case, MIPS emerges either upon increasing the Péclet number ℓ at fixed density or upon increasing the density at large ℓ (for fixed Stokes number St), reproducing the density-activity phase diagram reported in previous studies [see Figs. 2(a) and 2(b)]. No reentrance is observed when ℓ is further increased beyond the instability threshold, coherently with recent studies that attribute it to interaction softness [60,67].

The phase diagram in the plane of inertia and density (at fixed Péclet) shows the suppression of MIPS at large inertia [Fig. 2(b)], as previously seen in molecular dynamics [60] and experiments [59]. Interestingly, MIPS disappears in the overdamped limit, independently of the Enskog correction and choice of $\chi(\phi)$. This suppression originates from the lack of impenetrability: indeed, when impenetrability is enforced in the algorithm via backscattering (see EM), MIPS at small inertia is recovered [Figs. 2(c) and 2(d)]. Moreover, simulations with impenetrability display multiple clusters of finite size coherently with the binodal decomposition scenario [66].

Our comparative numerical analysis shows that impenetrability is essential in the overdamped regime to recover MIPS, in agreement with previous studies. By contrast, at large inertia, MIPS is observed even in the absence of impenetrability, indicating that the instability may originate from a different dynamical mechanism.

Kinetic theory—To investigate the dynamical origin of inertial MIPS, we develop a kinetic theory [71,72]. By coarse-graining the equations of motion, Eqs. (1) and (2), we obtain a kinetic equation for the evolution of the single-particle probability density $f = f(\mathbf{r}, \mathbf{v}, \mathbf{e}, t)$,

$$(\partial_t + \mathbf{v}\cdot\partial_{\mathbf{r}} + (\gamma/m)v_0\mathbf{e}\cdot\partial_{\mathbf{v}})f = (\mathcal{L}_b + \mathcal{L}_a)f + \mathcal{I}[f_2], \tag{4}$$

where the operators $\mathcal{L}_b$ and $\mathcal{L}_a$ represent the interaction with the bath and the active force dynamics, and $\mathcal{I}[f_2]$ describes the interparticle interactions. The latter term depends on the two-particle probability density $f_2 = f_2(\mathbf{r}_1, \mathbf{v}_1, \mathbf{e}_1, \mathbf{r}_2, \mathbf{v}_2, \mathbf{e}_2, t)$ (see EM). The crucial assumption in kinetic theories is to close Eq. (4) by expressing f_2 in terms of f. Here, consistently with the ADSMC algorithm, we adopt an Enskog-Boltzmann–like ansatz that incorporates density correlations at contact while replacing the hard-sphere collision frequency proportional to the relative velocity by a mean collision frequency proportional to the thermal velocity, as in the case of Maxwell molecules. Then, the collision operator takes the nonlinear form $\mathcal{I}[f_2] \to \mathcal{I}_B[f]$ with (see EM)

$$\mathcal{I}_B[f] = \nu \int d\mathbf{e}_1 d\mathbf{v}_1 d\hat{\boldsymbol{\sigma}}(\hat{b}_{\boldsymbol{\sigma}} - 1)f(\mathbf{r}, \mathbf{v}, \mathbf{e}, t)f(\mathbf{r}, \mathbf{v}_1, \mathbf{e}_1, t),$$

where $\nu = \nu(\mathbf{r}, t) = (\sigma/2)\sqrt{[T(\mathbf{r}, t)/m]}\chi[\phi(\mathbf{r}, t)]$ and the operator $\hat{b}_{\boldsymbol{\sigma}}$ transforms the velocities into the postcollisional velocities (see EM) when acting on functions of $(\mathbf{v}, \mathbf{v}_1)$ [73].

Spatially homogeneous stationary state—In the stationary and spatially homogeneous regime, the kinetic equation for the system admits a solution $f_s(\mathbf{v}, \mathbf{e})$ whose relevant moments can be theoretically evaluated (see EM). Thus, in what follows, averages refer to this particular state. From here, we can predict the correlation between velocity and orientation, $\langle \mathbf{e}\cdot\mathbf{v}\rangle$ (proportional to the active power), which is 0 in equilibrium when $v_0 = 0$. Out of equilibrium, when $v_0 > 0$ and $\tau > 0$ [74], we get (see EM) a closed equation for $z(n, T_0, v_0, \gamma, \tau, m) = \langle \mathbf{e}\cdot\mathbf{v}\rangle/v_0$:

$$\left[1 + \mathrm{St}^{-1} + \sqrt{2}\phi\chi(\phi)\ell(\tilde{T}_0 + z)^{1/2}\right]z = 2\mathrm{St}^{-1}, \tag{5}$$

where we introduce $T_a = mv_0^2/2$ and the rescaled thermal temperature $\tilde{T}_0 = T_0/T_a$ [75]. In the low density limit, one has $z \to [2/(1 + \mathrm{St})]$. Note that the knowledge of z gives also the knowledge of the stationary homogeneous temperature $\tilde{T}(\phi, \tilde{T}_0, \ell, \mathrm{St}) = T/T_a = \tilde{T}_0 + z(\phi, \tilde{T}_0, \ell, \mathrm{St})$. Crucially,

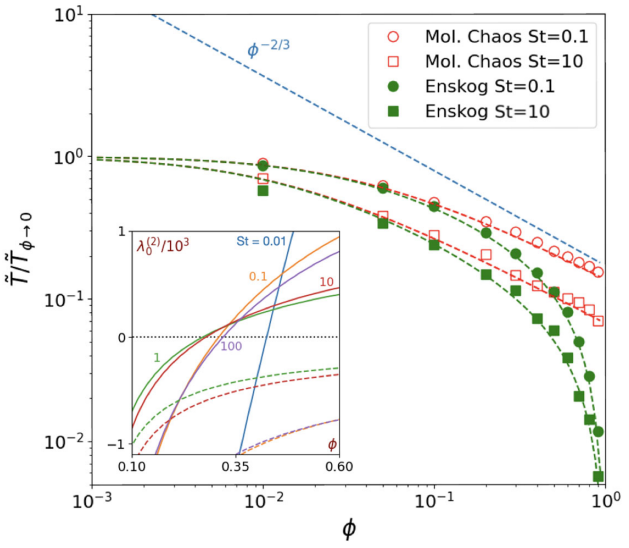

FIG. 3. Steady-state temperature $\tilde{T}$, normalized by its dilute-limit value $\tilde{T}_{\phi\to 0}$, as a function of the packing fraction ϕ for homogeneous configurations, demonstrating the cooling mechanism. Simulations are performed using both the molecular chaos (red) and Enskog (green) collision rates. Colored dashed lines indicate the corresponding theoretical predictions, while the light-blue dashed line serves as a guide to the eye for the scaling $\tilde{T} \approx z \sim \phi^{-2/3}$. Inset: theoretical prediction for the k^2 order contribution to the density eigenvalue $\lambda_0^{(2)}$ as a function of ϕ for Enskog (solid lines) and molecular chaos (dashed lines) collision rates. The colored numbers in the plot denote the Stokes number values. In all data, $\ell = 100$ and $\tilde{T}_0 = 2 \times 10^{-4}$. Note that St is varied by keeping $m = 1$ and $\tau = 1$ fixed while changing γ.

when $\tilde{T}_0 \ll 1$ (e.g., for large v_0), one has $\tilde{T} \approx z$, and Eq. (5) depends upon γ, m, τ, and v_0 only through St, ℓ: then, in the high density limit, $\tilde{T} \to [\sqrt{2}/(\mathrm{St}\sigma\ell)^{2/3}][\phi\chi(\phi)]^{-2/3}$. However, in general, the equation depends also on $\tilde{T}_0$, and therefore, scalings also should take this parameter into account. We are now in the position of quantifying how the temperature cools down with increasing density, even if the collisions are elastic. Notwithstanding this, when molecular chaos is strictly enforced, no phase separation can be observed, at odds with the phenomenology of cooling granular gases, where a spatially homogeneous state can be unstable even in the low density limit [68]. The crucial point is how fast T decays with ϕ. With cooling granular gases, one may have a (rescaled) decay faster than ϕ^{-1}, while here, with molecular chaos $\chi = 1$, the decay of the temperature is not faster than $\phi^{-2/3}$. As known since the general analysis by Cates and Tailleur [16], and confirmed below by our theory, this is not sufficient to observe MIPS. In Fig. 3, we show the decay of $\tilde{T} \approx z$ with molecular chaos and with the Enskog correction, comparing it with single-cell (homogeneous) ADSMC simulations, observing an excellent agreement without any adjustable parameter.

Density linear stability from the kinetic equation—Deviations of the probability density from the stationary spatially homogeneous solutions are indicated by $\delta f(\mathbf{r}, \mathbf{v}, \mathbf{e}, t) = f(\mathbf{r}, \mathbf{v}, \mathbf{e}, t) - f_s(\mathbf{v}, \mathbf{e})$. In the Supplemental Material (SM [76]), we show that δf obeys

$$\partial_t \delta f(\mathbf{r}, \mathbf{v}, \mathbf{e}, t) = [\Lambda(\mathbf{v}, \mathbf{e}) - \mathbf{v} \cdot \partial_{\mathbf{r}}]\delta f(\mathbf{r}, \mathbf{v}, \mathbf{e}, t), \quad (6)$$

where $\Lambda(\mathbf{v}, \mathbf{e})$ is the homogeneous linearized Boltzmann operator (see SM for its definition [77]). While an eigenvalue problem is defined for each Fourier mode $\delta f_k = \int d\mathbf{r} e^{-i\mathbf{k}\cdot\mathbf{r}} \delta f$, remarkably, we can identify the exact eigenfunction of Λ associated with the null eigenvalue. By assuming that the eigenvalues and eigenfunctions are analytic in k, and focusing on the one that vanishes for $k \to 0$ (that governs the dynamics in the long-time limit), we expand as $\lambda_{0,k} = ik\lambda_0^{(1)} + k^2\lambda_0^{(2)} + O(k^3)$, where we have set $\mathbf{k} = k\hat{x}$ by isotropy. As the problem is nondegenerate, perturbation theory allows us to find $\lambda_0^{(1)} = 0$ and

$$\frac{\lambda_0^{(2)}}{D_0} = -(1 + \mathrm{St}^{-1}) \frac{d}{d\phi}[\phi\tilde{T}(\phi, \tilde{T}_0, \ell, \mathrm{St})] + \mathrm{St}^{-1}\tilde{T}_0 \quad (7)$$

with $D_0 = T_a/\gamma$ (see SM [76]). The eigenvalue $\lambda_0^{(2)}$ needs to be negative to guarantee the linear stability of the homogeneous state. In the hydrodynamic limit $k \to 0, t \to \infty$ with $k^2 t$ finite, the above result implies that the density modes $n_k(t)$ (Fourier modes of the density field) evolve according to the diffusion equation

$$\partial_t n_k(t) = -D_{\mathrm{eff}} k^2 n_k(t) \quad (8)$$

with effective diffusion coefficient $D_{\mathrm{eff}} = -\lambda_0^{(2)}$. Note that the same result for the stability of the density field (and its ultimate diffusion evolution) can be obtained by expanding the kinetic equations for the hydrodynamic fields through the Chapman-Enskog method. The expressions in Eqs. (7) and (8) are valid also for hard sphere or disk collisional kernel, but explicit expressions for T and z are not analytically available without some kind of approximation of the kinetic equation. As mentioned before, when molecular chaos is enforced ($\chi = 1$), the decay of T with n is not fast enough to guarantee that D_{eff} becomes negative, i.e., instability is never observed. On the contrary, when Enskog correction is introduced ($\chi > 1$), MIPS appears for the parameter region such that $D_{\mathrm{eff}} < 0$ (inset of Fig. 3). While the route to phase separation mirrors that observed in cooling granular gases—namely, a coupling between temperature, pressure, and density—the underlying mechanism responsible for this coupling is different. In the present case, it is self-propulsion that is progressively weakened by the randomizing effect of collisions, giving rise to an effective, density-dependent cooling. This cooling mechanism is inherently less efficient than in granular gases, and therefore, requires enhancement, which

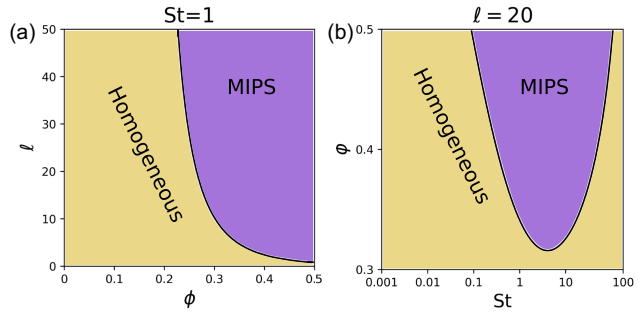

FIG. 4. Theoretical phase diagrams from Eq. (7). (a) Phase diagram in the plane of Péclet number ℓ and packing fraction ϕ at Stokes number $\mathrm{St} = 1$. (b) Phase diagram in the plane of ϕ and St at $\ell = 20$. The violet region (MIPS) highlights the region where the homogeneous density is unstable [$\lambda_0^{(2)} > 0$].

can be accounted for through an Enskog-type correction. The theory predicts phase diagrams in the plane of Péclet number and packing fraction ϕ [Fig. 4(a)] and in the plane of ϕ and Stokes number St [Fig. 4(b)] in fair agreement with those observed in ADSMC simulations [Figs. 2(a) and 2(b)]. In the high inertia limit $\mathrm{St} \to \infty$, MIPS disappears, since $z \to 0$ and $\lambda_0^{(2)} \to -D_0\tilde{T}_0$, in agreement with previous numerical and experimental results [59–61]. As in ADSMC simulations, MIPS is suppressed in the overdamped limit $\mathrm{St} \to 0$, because the homogeneous density is stable, $z \to 2$, and $\lambda_0^{(2)} \to -2\mathrm{St}^{-1}$. This artifact is due to the lack of impenetrability in the theory. In fact, when ADSMC is performed with backscattering (impenetrability), MIPS reappears for $\mathrm{St} \to 0$, as expected for overdamped active systems.

Conclusions—We have shown that inertial MIPS arises from a kinetic temperature decrease with density (cooling), which differs from the density-dependent speed reduction typical of overdamped active matter. In our case, temperature and macroscopic velocity are independent fields. However, alternative definitions of temperature [78]—such as effective temperatures based on fluctuation-dissipation relation violations [79] or extensions to two dimensions of the analytical approach developed by Akintunde *et al.* [80]—may provide a promising route to complement our theoretical framework.

The observed cooling mechanism is reminiscent of the clustering in granular materials governed by dissipative interactions [68]. However, unlike in that case, the present instability requires an Enskog–like correction to the collision rate, going beyond the molecular chaos hypothesis. This correlation-induced enhancement of collisions couples density, orientation, and temperature, giving rise to the cooling mechanism responsible for phase separation. Inferring such a correction directly from simulations could provide a first step toward extending the present theory from hard spheres to systems with soft interactions.

Our findings are supported by simulations performed through an active direct Monte Carlo method inspired by the Bird algorithm for molecular and granular gases. This numerical technique could be generalized to the overdamped limit by starting from the Boltzmann–like equation proposed in Ref. [32] for overdamped active particles. Importantly, our algorithm is faster than molecular dynamics simulations (see EM for details) and avoids the critical time-step limitations of previous Monte Carlo approaches [81,82]. As such, it may represent a new paradigm for large-scale active matter simulations, capable of incorporating off-centered collisions that produce torques in chiral active matter [83] and tangential forces responsible for self-alignment [84].

Acknowledgments—M. M., M. I. G. d. S., and P. M. acknowledge the support of Grant No. ProyExcel-00505, funded by the Junta de Andalucía, and Grant No. PID2021-126348NB-I00, funded by MCIN/AEI/10.13039/501100011033 and ERDF, "A way of making Europe." L. C. and A. P. acknowledge funding from the Italian Ministero dell'Università e della Ricerca under the program PRIN 2022 ("reranking of the final lists"), No. 2022 KWTEB7, cup No. B53C24006470006.

Data availability—The data that support the findings of this article are openly available [85].

[1] M. C. Marchetti, J. F. Joanny, S. Ramaswamy, T. B. Liverpool, J. Prost, M. Rao, and R. A. Simha, Hydrodynamics of soft active matter, Rev. Mod. Phys. **85**, 1143 (2013).
[2] J. Elgeti, R. G. Winkler, and G. Gompper, Physics of microswimmers—Single particle motion and collective behavior: A review, Rep. Prog. Phys. **78**, 056601 (2015).
[3] C. Bechinger, R. Di Leonardo, H. Löwen, C. Reichhardt, G. Volpe, and G. Volpe, Active particles in complex and crowded environments, Rev. Mod. Phys. **88**, 045006 (2016).
[4] R. G. Winkler and G. Gompper, The physics of active polymers and filaments, J. Chem. Phys. **153**, 040901 (2020).
[5] B. Nath, L. Caprini, C. Maggi, A. Zizzari, V. Arima, I. Viola, R. Di Leonardo, and A. Puglisi, A microfluidic method for passive trapping of sperms in microstructures, Lab Chip **23**, 773 (2023).
[6] R. Di Leonardo, L. Angelani, D. Dell'Arciprete, G. Ruocco, V. Iebba, S. Schippa, M. P. Conte, F. Mecarini, F. De Angelis, and E. Di Fabrizio, Bacterial ratchet motors, Proc. Natl. Acad. Sci. U.S.A. **107**, 9541 (2010).
[7] J. Arlt, V. A. Martinez, A. Dawson, T. Pilizota, and W. C. Poon, Painting with light-powered bacteria, Nat. Commun. **9**, 768 (2018).
[8] I. Buttinoni, J. Bialké, F. Kümmel, H. Löwen, C. Bechinger, and T. Speck, Dynamical clustering and phase separation in suspensions of self-propelled colloidal particles, Phys. Rev. Lett. **110**, 238301 (2013).
[9] A. Bricard, J.-B. Caussin, N. Desreumaux, O. Dauchot, and D. Bartolo, Emergence of macroscopic directed motion in populations of motile colloids, Nature (London) **503**, 95 (2013).

[10] A. Cavagna and I. Giardina, Bird flocks as condensed matter, Annu. Rev. Condens. Matter Phys. **5**, 183 (2014).
[11] M. Moussaïd, N. Perozo, S. Garnier, D. Helbing, and G. Theraulaz, The walking behaviour of pedestrian social groups and its impact on crowd dynamics, PLoS One **5**, e10047 (2010).
[12] M. Leyman, F. Ogemark, J. Wehr, and G. Volpe, Tuning phototactic robots with sensorial delays, Phys. Rev. E **98**, 052606 (2018).
[13] M. Agrawal and S. C. Glotzer, Scale-free, programmable design of morphable chain loops of kilobots and colloidal motors, Proc. Natl. Acad. Sci. U.S.A. **117**, 8700 (2020).
[14] G. Vásárhelyi, C. Virágh, G. Somorjai, T. Nepusz, A. E. Eiben, and T. Vicsek, Optimized flocking of autonomous drones in confined environments, Sci. Rob. **3**, eaat3536 (2018).
[15] J. O'Byrne, Y. Kafri, J. Tailleur, and F. van Wijland, Time irreversibility in active matter, from micro to macro, Nat. Rev. Phys. **4**, 167 (2022).
[16] M. E. Cates and J. Tailleur, Motility-induced phase separation, Annu. Rev. Condens. Matter Phys. **6**, 219 (2015).
[17] G. Gonnella, D. Marenduzzo, A. Suma, and A. Tiribocchi, Motility-induced phase separation and coarsening in active matter, C.R. Phys. **16**, 316 (2015).
[18] J. Bialké, T. Speck, and H. Löwen, Active colloidal suspensions: Clustering and phase behavior, J. Non-Cryst. Solids **407**, 367 (2015).
[19] Y. Fily and M. C. Marchetti, Athermal phase separation of self-propelled particles with no alignment, Phys. Rev. Lett. **108**, 235702 (2012).
[20] G. S. Redner, M. F. Hagan, and A. Baskaran, Structure and dynamics of a phase-separating active colloidal fluid, Phys. Rev. Lett. **110**, 055701 (2013).
[21] D. Levis, J. Codina, and I. Pagonabarraga, Active Brownian equation of state: Metastability and phase coexistence, Soft Matter **13**, 8113 (2017).
[22] P. Digregorio, D. Levis, A. Suma, L. F. Cugliandolo, G. Gonnella, and I. Pagonabarraga, Full phase diagram of active brownian disks: From melting to motility-induced phase separation, Phys. Rev. Lett. **121**, 098003 (2018).
[23] S. Hermann, D. de Las Heras, and M. Schmidt, Nonnegative interfacial tension in phase-separated active Brownian particles, Phys. Rev. Lett. **123**, 268002 (2019).
[24] T. Speck, Collective behavior of active Brownian particles: From microscopic clustering to macroscopic phase separation, Eur. Phys. J. Special Topics **225**, 2287 (2016).
[25] J. U. Klamser, S. C. Kapfer, and W. Krauth, Thermodynamic phases in two-dimensional active matter, Nat. Commun. **9**, 5045 (2018).
[26] L. Caprini, U. Marini Bettolo Marconi, and A. Puglisi, Spontaneous velocity alignment in motility-induced phase separation, Phys. Rev. Lett. **124**, 078001 (2020).
[27] S. Bröker, J. Bickmann, M. Te Vrugt, M. E. Cates, and R. Wittkowski, Orientation-dependent propulsion of active brownian spheres: From self-advection to programmable cluster shapes, Phys. Rev. Lett. **131**, 168203 (2023).
[28] R. F.-Q. García, E. Chacón, P. Tarazona, and C. Valeriani, Dynamics and rupture of doped motility induced phase separation, Soft Matter **21**, 5413 (2025).
[29] R. Wittmann, C. Maggi, A. Sharma, A. Scacchi, J. M. Brader, and U. M. B. Marconi, Effective equilibrium states in the colored-noise model for active matter I. Pairwise forces in the fox and unified colored noise approximations, J. Stat. Mech. (2017) P113207.
[30] A. P. Solon, J. Stenhammar, R. Wittkowski, M. Kardar, Y. Kafri, M. E. Cates, and J. Tailleur, Pressure and phase equilibria in interacting active Brownian spheres, Phys. Rev. Lett. **114**, 198301 (2015).
[31] A. K. Omar, H. Row, S. A. Mallory, and J. F. Brady, Mechanical theory of nonequilibrium coexistence and motility-induced phase separation, Proc. Natl. Acad. Sci. U.S.A. **120**, e2219900120 (2023).
[32] R. Soto, M. Pinto, and R. Brito, Kinetic theory of motility induced phase separation for active Brownian particles, Phys. Rev. Lett. **132**, 208301 (2024).
[33] H. Löwen, Inertial effects of self-propelled particles: From active Brownian to active Langevin motion, J. Chem. Phys. **152**, 040901 (2020).
[34] P. Baconnier, D. Shohat, C. H. López, C. Coulais, V. Démery, G. Düring, and O. Dauchot, Selective and collective actuation in active solids, Nat. Phys. **18**, 1234 (2022).
[35] F. Siebers, A. Jayaram, P. Blümler, and T. Speck, Exploiting compositional disorder in collectives of light-driven circle walkers, Sci. Adv. **9**, eadf5443 (2023).
[36] K. Engbring, D. Boriskovsky, Y. Roichman, and B. Lindner, A nonlinear fluctuation-dissipation test for Markovian systems, Phys. Rev. X **13**, 021034 (2023).
[37] M. Casiulis, E. Arbel, Y. Lahini, S. Martiniani, N. Oppenheimer, and M. Y. B. Zion, A geometric condition for robot-swarm cohesion and cluster-flock transition, Proc. Natl. Acad. Sci. U.S.A. **122**, e2502211122 (2025).
[38] I. S. Aranson, D. Volfson, and L. S. Tsimring, Swirling motion in a system of vibrated elongated particles, Phys. Rev. E **75**, 051301 (2007).
[39] A. Kudrolli, G. Lumay, D. Volfson, and L. S. Tsimring, Swarming and swirling in self-propelled polar granular rods, Phys. Rev. Lett. **100**, 058001 (2008).
[40] J. Deseigne, O. Dauchot, and H. Chaté, Collective motion of vibrated polar disks, Phys. Rev. Lett. **105**, 098001 (2010).
[41] N. Kumar, H. Soni, S. Ramaswamy, and A. Sood, Flocking at a distance in active granular matter, Nat. Commun. **5**, 4688 (2014).
[42] N. Koumakis, A. Gnoli, C. Maggi, A. Puglisi, and R. Di Leonardo, Mechanism of self-propulsion in 3D-printed active granular particles, New J. Phys. **18**, 113046 (2016).
[43] A. P. Antonov, L. Caprini, A. Ldov, C. Scholz, and H. Löwen, Inertial active matter with coulomb friction, Phys. Rev. Lett. **133**, 198301 (2024).
[44] C. Scholz, M. Engel, and T. Pöschel, Rotating robots move collectively and self-organize, Nat. Commun. **9**, 931 (2018).
[45] M. Workamp, G. Ramirez, K. E. Daniels, and J. A. Dijksman, Symmetry-reversals in chiral active matter, Soft Matter **14**, 5572 (2018).
[46] M. López-Castaño, J. F. González-Saavedra, A. Rodríguez-Rivas, E. Abad, S. B. Yuste, and F. Vega Reyes, Pseudo-two-dimensional dynamics in a system of macroscopic rolling spheres, Phys. Rev. E **103**, 042903 (2021).
[47] M. A. López-Castaño, A. Marquez Seco, A. Marquez Seco, A. Rodriguez-Rivas, and F. V. Reyes, Chirality transitions in

a system of active flat spinners, Phys. Rev. Res. **4**, 033230 (2022).
[48] J. Rabault, R. A. Fauli, and A. Carlson, Curving to fly: Synthetic adaptation unveils optimal flight performance of whirling fruits, Phys. Rev. Lett. **122**, 024501 (2019).
[49] H. Mukundarajan, T. C. Bardon, D. H. Kim, and M. Prakash, Surface tension dominates insect flight on fluid interfaces, J. Exp. Biol. **219**, 752 (2016).
[50] S. C. Takatori and J. F. Brady, Inertial effects on the stress generation of active fluids, Phys. Rev. Fluids **2**, 094305 (2017).
[51] C. Scholz, S. Jahanshahi, A. Ldov, and H. Löwen, Inertial delay of self-propelled particles, Nat. Commun. **9**, 5156 (2018).
[52] M. Leoni, M. Paoluzzi, S. Eldeen, A. Estrada, L. Nguyen, M. Alexandrescu, K. Sherb, and W. W. Ahmed, Surfing and crawling macroscopic active particles under strong confinement: Inertial dynamics, Phys. Rev. Res. **2**, 043299 (2020).
[53] L. Caprini and U. Marini Bettolo Marconi, Inertial self-propelled particles, J. Chem. Phys. **154**, 024902 (2021).
[54] G. P. Nguyen, R. Wittmann, and H. Löwen, Active ornstein–uhlenbeck model for self-propelled particles with inertia, J. Phys. USSR **34**, 035101 (2021).
[55] S. De Karmakar, A. Chugh, and R. Ganesh, Collective behavior of soft self-propelled disks with rotational inertia, Sci. Rep. **12**, 22563 (2022).
[56] N. P. Kryuchkov, A. D. Nasyrov, K. D. Gursky, and S. O. Yurchenko, Inertia changes evolution of motility-induced phase separation in active matter across particle activity, Phys. Rev. E **107**, 044601 (2023).
[57] A. Deblais, T. Barois, T. Guerin, P.-H. Delville, R. Vaudaine, J. S. Lintuvuori, J.-F. Boudet, J.-C. Baret, and H. Kellay, Boundaries control collective dynamics of inertial self-propelled robots, Phys. Rev. Lett. **120**, 188002 (2018).
[58] A. P. Antonov, M. Musacchio, H. Löwen, and L. Caprini, Self-sustained frictional cooling in active matter, Nat. Commun. **16**, 7235 (2025).
[59] L. Caprini, D. Breoni, A. Ldov, C. Scholz, and H. Löwen, Dynamical clustering and wetting phenomena in inertial active matter, Commun. Phys. **7**, 343 (2024).
[60] S. Mandal, B. Liebchen, and H. Löwen, Motility-induced temperature difference in coexisting phases, Phys. Rev. Lett. **123**, 228001 (2019).
[61] S. De Karmakar and R. Ganesh, Motility-induced phase separation of self-propelled soft inertial disks, Soft Matter **18**, 7301 (2022).
[62] D. Horvath, C. Slabý, Z. Tomori, A. Hovan, P. Miskovsky, and G. Bánó, Bouncing dynamics of inertial self-propelled particles reveals directional asymmetry, Phys. Rev. E **107**, 024603 (2023).
[63] L. Caprini, A. Ldov, R. K. Gupta, H. Ellenberg, R. Wittmann, H. Löwen, and C. Scholz, Emergent memory from tapping collisions in active granular matter, Commun. Phys. **7**, 52 (2024).
[64] L. Hecht, S. Mandal, H. Löwen, and B. Liebchen, Active refrigerators powered by inertia, Phys. Rev. Lett. **129**, 178001 (2022).
[65] C. Dai, I. R. Bruss, and S. C. Glotzer, Phase separation and state oscillation of active inertial particles, Soft Matter **16**, 2847 (2020).
[66] J. Su, H. Jiang, and Z. Hou, Inertia-induced nucleation-like motility-induced phase separation, New J. Phys. **23**, 013005 (2021).
[67] J. Feng and A. K. Omar, Theory for the anomalous phase behavior of inertial active Brownian particles, Phys. Rev. E **111**, L043402 (2025).
[68] I. Goldhirsch and G. Zanetti, Clustering instability in dissipative gases, Phys. Rev. Lett. **70**, 1619 (1993).
[69] P. Maynar, M. I. García de Soria, and J. J. Brey, Understanding an instability in vibrated granular monolayers, Phys. Rev. E **99**, 032903 (2019).
[70] We note that our choice of $\chi(\phi)$, related to the Carnahan-Starling expression, is natural for our simulations and theory, which are formulated for hard spheres. Alternative forms of $\chi(\phi)$ could be considered upon extending the theory to systems with soft interactions.
[71] A. Baskaran, J. W. Dufty, and J. J. Brey, Transport coefficients for the hard-sphere granular fluid, Phys. Rev. E **77**, 031311 (2008).
[72] N. V. Brilliantov and T. Pöschel, *Kinetic Theory of Granular Gases* (Oxford University Press, New York, 2010).
[73] The $1/2$ factor in ν corresponds to the correct choice for comparison with ADSMC simulations.
[74] In general, an out-of-equilibrium passive liquid has $v_0 \geq 0$ and $\tau \geq 0$, while $v_0 = 0$ and $\tau \to 0$ hold for passive systems.
[75] See EM, Physical Units, for a discussion of the Péclet number.
[76] See Supplemental Material at http://link.aps.org/supplemental/10.1103/mbrl-v75b for details about derivation of the diffusion equation from kinetic theory.
[77] Here, $[x]$ stands for the average integer part of its real argument x, that is, $\lfloor x \rfloor + s$, where s is a random variable that can take value 1 with probability $x - \lfloor x \rfloor$ and 0 otherwise ($\lfloor x \rfloor$ is the truncated or floor integer part of x).
[78] L. Hecht, L. Caprini, H. Löwen, and B. Liebchen, How to define temperature in active systems?, J. Chem. Phys. **161**, 224904 (2024).
[79] D. Loi, S. Mossa, and L. F. Cugliandolo, Effective temperature of active complex matter, Soft Matter **7**, 3726 (2011).
[80] A. Akintunde, P. Bayati, H. Row, and S. A. Mallory, Single-file diffusion of active Brownian particles, J. Chem. Phys. **162**, 164902 (2025).
[81] D. Levis and L. Berthier, Clustering and heterogeneous dynamics in a kinetic Monte Carlo model of self-propelled hard disks, Phys. Rev. E **89**, 062301 (2014).
[82] J. U. Klamser, O. Dauchot, and J. Tailleur, Kinetic monte carlo algorithms for active matter systems, Phys. Rev. Lett. **127**, 150602 (2021).
[83] L. Caprini and U. Marini Bettolo Marconi, Bubble phase induced by odd interactions in chiral systems, J. Chem. Phys. **162**, 161101 (2025).
[84] P. Baconnier, O. Dauchot, V. Démery, G. Düring, S. Henkes, C. Huepe, and A. Shee, Self-aligning polar active matter, Rev. Mod. Phys. **97**, 015007 (2025).
[85] A. Puglisi (2026), 10.5281/zenodo.19495697.

[86] G. A. Bird, *Molecular Gas Dynamics and the Direct Simulation of Gas Flows* (Oxford University Press, New York, 1994).

[87] C. Cercignani, R. Illner, and M. Pulvirenti, *The Mathematical Theory of Dilute Gases* (Springer Science & Business Media, New York, 2013), Vol. 106.

End Matter

Active direct simulation Monte Carlo—In the free streaming step, the equations of motion are integrated from $t_i = idt$ to $t_{i+1} = t_i + dt$, ignoring possible interactions, i.e., setting $\mathbf{f}_\mathbf{i}^{\mathbf{int}} = 0$. For the system under consideration, the free streaming step consists in evolving the three vectors for each particle, $\{\mathbf{r}, \mathbf{v}, \mathbf{e}\}$. In the following, we show results obtained by employing the Euler-Maruyama integration method, including the stochastic terms at order $\sqrt{dt}$. During the interaction phase, in each cell, a "particle-particle" collision step is operated. When impenetrability (BS) is implemented, a second "backscattering collision" step is also applied.

The particle-particle collisions are treated by first computing the number of expected colliding pairs according to the following formula [77]:

$$n_{\mathrm{coll}} = \left[\frac{dt}{t_{\mathrm{coll}}}\right]\tilde{N}, \tag{A1}$$

where $\tilde{N}$ is the number of particles in the cell. The term t_{coll} is the estimated mean free time determined according to the Enskog-Maxwell-Boltzmann formula $t_{\mathrm{coll}} = [\chi(\phi)\sigma n\bar{v}]^{-1}$, where σ denotes the particle diameter, $n = \tilde{N}/\Delta^2$ represents the local density of particles, $\phi = n\pi\sigma^2/4$ is the local packing fraction, and $\bar{v}$ corresponds to the typical particle speed in the cell, defined as $\bar{v} = \sqrt{\langle|\mathbf{v} - \langle\mathbf{v}\rangle|^2\rangle}$. Here, averages are restricted to the cell (and if $\tilde{N} \leq 1$, no collisions are computed). Once the expected number of collisions, n_{coll}, has been determined, a cycle is performed for n_{coll} steps: in each step, two particles i, j are randomly chosen in the cell, and their velocities are updated according to the following elastic collision rule that conserves momentum and kinetic energy:

$$\mathbf{v}_i' = \mathbf{v}_i - (\Delta\mathbf{v}\cdot\hat{n})\hat{n}, \tag{A2}$$

$$\mathbf{v}_j' = \mathbf{v}_j + (\Delta\mathbf{v}\cdot\hat{n})\hat{n}, \tag{A3}$$

where $\Delta\mathbf{v} = \mathbf{v}_i - \mathbf{v}_j$ and $\hat{n} = [\cos(\beta), \sin(\beta)]$, with β extracted from a uniform probability distribution between 0 and 2π, and prime indicates postcollisional velocities. The crucial assumption of this integration scheme is that particle positions within a cell are ignored when evaluating interactions. This is equivalent to performing a Monte Carlo approximation of the collisional integral $I[f|f]$. By setting $\chi = 1$, one recovers the ADSMC scheme under molecular chaos, which, for passive particles, is known to converge to the solution of the Boltzmann equation. In our implementation, we employ the Carnahan-Starling approximation, $\chi = (1 - 7\phi/16)/(1 - \phi)^2$.

The backscattering effect affects every particle of the cell that, during its previous movement, has moved to a different cell where there is already a number of particles, $\tilde{N}_{\max}$ (e.g., in two dimensions, we use $\tilde{N}_{\max} = \lceil\Delta^2/(\pi\sigma^2/4)\rceil$): in that case, the particle is "bounced back" to a uniformly random position of the cell of origin with a uniformly random rotation of the velocity vector.

Virtual number of particles—The choice of small Δ (usually of the order of a few diameters) leads to important finite size effects in the interaction step, in particular, too frequent repeated collisions, leading to discrepancies with the kinetic theory. Another finite size effect is the possibility of unrealistic local fluctuations of the packing fraction with $\phi > 1$: even if this happens rarely, it affects drastically the implementation of the Carnahan-Starling $\chi(\phi)$ recipe, which diverges at $\phi = 1$.

In the usual application of the DSMC [86,87], the number of simulated particles does not correspond to the real physical number. For molecular systems, this "virtual number" is much smaller than the (typically huge) physical number. In granular gas applications, on the contrary, finite size effects are usually dealt with by considering a larger number of virtual particles, $N_v = \beta N$ particles, with $\beta > 1$. This is our choice for ADSMC. The interaction step is then performed by considering the physical (not virtual) local packing fraction, ϕ/β, for the purpose of computing the local collision time, t_{coll}: this means that each particle collides a number of times according to the physical and not the virtual local density. The large number of virtual particles, however, reduces spurious repeated collisions and nonphysical density fluctuations.

In the results of Fig. 2, we have used $\beta = 5$. When $\beta = 1$ is used, the ADSMC cannot be implemented without BS because of the aforementioned problem of packing fraction fluctuations. Even when $\beta > 1$, the simulations without BS can present (very rare) fluctuations with local $\phi > 1$; we have coped with this problem by regularizing $\chi(\phi)$, i.e., by using the Carnahan-Starling formula for $\phi \leq \phi^*$ and $\chi(\phi) = \chi(\phi^*)$ with $\phi^* = 0.95$.

Physical units—There are six parameters: $m, \tau, \gamma, T_0, v_0, \sigma$. We have defined three adimensional parameters: $\tilde{T}_0 = T_0/(mv_0^2/2)$, $\mathrm{St} = m/(\tau\gamma)$, and $\ell = \tau v_0/\sigma$. If the three fundamental units for time, length, and energy are taken to be $\tau = 1$, $\sigma = 1$, and $T_0 = 1$, then the

knowledge of the three adimensional parameters gives immediate knowledge of the three dimensional nonunitary parameters: $v_0 = \ell$, $m = 2/(\tilde{T}_0\ell^2)$, and $\gamma = 2/(\tilde{T}_0\ell^2\mathrm{St})$. With this way of defining units, changes in St are equivalent to changes in γ. Note that $\ell = \tau v_0/\sigma$ can be considered a Péclet number: it is in fact (apart from a factor of 2) equivalent to the ratio between the rescaled ballistic time $(\sigma/v_0)/\tau$ and the rescaled diffusion time $(\sigma^2/D_a)/\tau$ with $D_a = T_a\tau$.

Computational advantage of ADSMC—For the same physical parameters, the time step required in molecular dynamics (MD) simulations is typically 10^2–10^3 times smaller than in ADSMC, resulting in a comparable computational speedup. This difference arises from the distinct stability constraints: in MD, the time step must resolve the phase-space dynamics and is limited by $\min(\Delta x/v, \Delta v/a)$, where Δx and Δv are the required spatial and velocity resolutions, and v and a are typical velocities and accelerations. In contrast, ADSMC does not require the temporal resolution needed to compute forces and instantaneous velocities and is limited only by the smallest physical timescale, i.e., the mean free time τ or the inertial time m/γ.

Expressions for the kinetic operators and equations—The explicit expressions for the kinetic operators of Eq. (4) in the main text are

$$\mathcal{L}_b f(\mathbf{r},\mathbf{v},\mathbf{e},t) = \frac{\gamma}{m}\partial_{\mathbf{v}}\cdot\left(\frac{T_0}{m}\partial_{\mathbf{v}} + \boldsymbol{\nu}\right) f(\mathbf{r},\mathbf{v},\mathbf{e},t), \quad \text{(E1)}$$

$$\mathcal{L}_a f(\mathbf{r},\mathbf{v},\mathbf{e},t) = \frac{1}{\tau}\partial_{\mathbf{e}}\cdot(\mathbf{e}+\partial_{\mathbf{e}}) f(\mathbf{r},\mathbf{v},\mathbf{e},t), \quad \text{(E2)}$$

$$\mathcal{I}[f_2] = \sigma\int d\mathbf{e}_1\int d\mathbf{v}_1\int d\hat{\boldsymbol{\sigma}}|\mathbf{g}\cdot\hat{\boldsymbol{\sigma}}| \times[\Theta(\mathbf{g}\cdot\hat{\boldsymbol{\sigma}})\hat{b}_{\boldsymbol{\sigma}} - \Theta(-\mathbf{g}\cdot\hat{\boldsymbol{\sigma}})] f_2(\mathbf{r},\mathbf{v},\mathbf{e},\mathbf{r}+\boldsymbol{\sigma},\mathbf{v}_1,\mathbf{e}_1,t), \quad \text{(E3)}$$

where $\mathbf{g} \equiv \mathbf{v}_1 - \mathbf{v}$ is the relative velocity, $\boldsymbol{\sigma}$ is a vector joining the two particles at contact (pointing away from the particle with velocity $\mathbf{v}$), and $\hat{\boldsymbol{\sigma}} \equiv \boldsymbol{\sigma}/\sigma$. The operator $\hat{b}_{\boldsymbol{\sigma}}$ transforms precollisional velocities $(\mathbf{v},\mathbf{v}_1)$ into their postcollisional values, i.e., $\hat{b}_{\boldsymbol{\sigma}} g(\mathbf{v},\mathbf{v}_1) = g(\hat{b}_{\boldsymbol{\sigma}}\mathbf{v}, \hat{b}_{\boldsymbol{\sigma}}\mathbf{v}_1)$, with $\hat{b}_{\boldsymbol{\sigma}}\mathbf{v} = \mathbf{v} + (\mathbf{g}\cdot\hat{\boldsymbol{\sigma}})\hat{\boldsymbol{\sigma}}$, $\hat{b}_{\boldsymbol{\sigma}}\mathbf{v}_1 = \mathbf{v}_1 - (\mathbf{g}\cdot\hat{\boldsymbol{\sigma}})\hat{\boldsymbol{\sigma}}$.

Assuming molecular chaos for precollisional velocities while retaining positional correlations, the two-particle distribution function can be approximated as

$$f_2(\mathbf{r},\mathbf{v},\mathbf{e},\mathbf{r}+\boldsymbol{\sigma},\mathbf{v}_1,\mathbf{e}_1,t) = \chi[\phi] f(\mathbf{r},\mathbf{v},\mathbf{e},t) \times f(\mathbf{r}+\boldsymbol{\sigma},\mathbf{v}_1,\mathbf{e}_1,t), \quad \text{(E4)}$$

where $\chi[\phi] = \chi[\phi(\mathbf{r},t)]$ is the density-dependent pair correlation function at contact. If Eq. (E4) is substituted in Eq. (E3), we obtain the Enskog collision operator,

$$\mathcal{I}_E[f] = \sigma\int d\mathbf{e}_1\int d\mathbf{v}_1\int d\hat{\boldsymbol{\sigma}}|\mathbf{g}\cdot\hat{\boldsymbol{\sigma}}|\chi[\phi] \times[\Theta(\mathbf{g}\cdot\hat{\boldsymbol{\sigma}})\hat{b}_{\boldsymbol{\sigma}} - \Theta(-\mathbf{g}\cdot\hat{\boldsymbol{\sigma}})] f(\mathbf{r},\mathbf{v},\mathbf{e},t) \times f(\mathbf{r}+\boldsymbol{\sigma},\mathbf{v}_1,\mathbf{e}_1,t). \quad \text{(E5)}$$

Finally, if the single-particle distribution varies weakly over distances of order σ, and assuming a velocity-independent collision frequency proportional to the local thermal speed—as in the simulations—one may replace $|\mathbf{g}\cdot\hat{\boldsymbol{\sigma}}| \to (1/2)\sqrt{[T(\mathbf{r},t)/m]}$ in Eq. (E5). Under this approximation, the form $\mathcal{I}_B[f]$ in the main text is recovered.

Homogeneous stationary state—To analyze the stationary state, we define the global moments in this state. For a microscopic function $\psi(\mathbf{v},\mathbf{e})$, its average is defined as

$$\langle\psi(\mathbf{v},\mathbf{e})\rangle \equiv \frac{1}{n}\int d\mathbf{e}\int d\mathbf{v}\psi(\mathbf{v},\mathbf{e}) f_s(\mathbf{v},\mathbf{e}), \quad \text{(F1)}$$

where $f_s(\mathbf{v},\mathbf{e})$ is the homogeneous stationary distribution function of the Boltzmann-Fokker-Planck equation.

To characterize the stationary state, we derive equations for the mixed and orientational correlators, $\langle e_i v_j\rangle$, $\langle e_i e_j\rangle$, and stationary temperature $T \equiv (m/2)\langle v^2\rangle$. This is done by multiplying Eq. (4), evaluated at the stationary distribution f_s (so that $\partial_t f_s = \partial_{\mathbf{r}} f_s = 0$), by $e_i v_j$, $e_i e_j$, and v^2, respectively, and integrating over $\mathbf{e}$ and $\mathbf{v}$. In this procedure, the collision integral is treated under the Enskog-Boltzmann molecular chaos assumption. Together with the stationary temperature condition, this procedure yields

$$\langle e_i e_j\rangle = \delta_{ij}, \quad \text{(F2a)}$$

$$T = T_0 + \frac{m}{2}v_0\langle\mathbf{e}\cdot\mathbf{v}\rangle, \quad \text{(F2b)}$$

$$\langle e_i v_j\rangle\left[\frac{\gamma}{m} + \tau^{-1} + \frac{\pi}{2}n\sigma\chi(n)\sqrt{T/m}\right] = \frac{2\gamma}{m}v_0\delta_{ij}. \quad \text{(F2c)}$$

Using the relation between packing fraction and density, Eq. (F2c) simplifies to $\langle e_i v_j\rangle = 0$ for $i \neq j$ and

$$\left[\frac{\gamma}{m} + \tau^{-1} + \Delta\left(\frac{2T_0}{m} + v_0\langle\mathbf{e}\cdot\mathbf{v}\rangle\right)^{1/2}\right]\langle\mathbf{e}\cdot\mathbf{v}\rangle = \frac{2\gamma}{m}v_0, \quad \text{(F3)}$$

with $\Delta = [\sqrt{2}\phi\chi(\phi)/\sigma]$. From here, Eq. (5) directly follows.

By direct derivation of Eq. (5) in the homogeneous state, we get an equation for $y = (d/d\phi)(\phi\tilde{T})$, which is central for the knowledge of the density eigenvalue $\lambda_0^{(2)}$; see Eq. (7). This equation is linear in y, leading immediately to

$$\frac{d}{d\phi}(\phi\tilde{T}) = -\frac{\sqrt{2}\ell \mathrm{St} z[\phi\chi'(\phi) + \chi(\phi)](z + \tilde{T}_0)}{(\sqrt{2}/2)\ell\phi \mathrm{St}\chi(\phi)(3z + 2\tilde{T}_0) + (\mathrm{St} + 1)\sqrt{z + \tilde{T}_0}}. \tag{F4}$$